SAND2023-04279C

Proceedings of the 20th International
Symposium on the Packaging and
Transportation of Radioactive Materials

PATRAM22

11-15 June 2023, Juan-les-Pins, France

DEVELOPMENT OF A DUCTILE RUPTURE FAILURE SURFACE FOR A HIGH-STRENGTH STEEL USING THE XUE-WIERZBICKI FAILURE MODEL

John L. Bignell
Sandia National Laboratories[1]

Robert J. Kalan
Sandia National Laboratories[1]

Douglas J. Ammerman
Sandia National Laboratories[1]

ABSTRACT

The ability to model ductile rupture in metal parts is critical in high stress applications. The initiation of ductile fracture is a function of the plastic strain, the stress state, and stress history. This paper develops a ductile rupture failure surface for precipitation hardened XM-13 (UNS 13800) condition H950 steel using the Xue-Wierzbicki failure model. The model is developed using data from five tensile specimen tests conducted at -40 ºC and 20 ºC. The specimens are designed to cover a Lode parameter range of 0.0 and 1.0 with a stress triaxiality range from 0.0 in pure shear to approximately 1.0 in tension. The failure surface can be implemented directly in a finite element code or used as a post processing check. The method used to develop this failure surface can be applied to other grades of steel that experience ductile failure when loaded due to extreme events. This can have application in the analysis of radioactive material shipping packages when exposed to extra-regulatory impacts or to sacrificial components of packages when loaded by the hypothetical accident conditions.

INTRODUCTION

Failure of metal parts by ductile rupture is of concern in many engineering applications. The work described in this paper was performed to support the assessment of a precipitation hardened XM-13 (UNS 13800) condition H950 stainless steel (PH13-8Mo H950) containment vessel for ductile rupture resulting from loads derived from hypothetical accident conditions (HACs) described in Title 10 of the Code of Federal Regulations, Part 71 (10 CFR 71) Packaging and Transportation of Radioactive Material.

Ductile rupture in metals is complex and a function of plastic strain, stress state, and the history of those variables. Bridgman performed the seminal work on the effects of stress state on ductile rupture in the 1940's and 1950's [1]. His work showed that the fracture strain in steels increases with decreasing mean stress σ_m. The mean stress is defined as equal to $I_1/3$, where I_1 is the first invariant of the Cauchy stress tensor. Subsequent work by Johnson and Cook incorporated this

---

[1] Sandia National Laboratories is a multimission laboratory managed and operated by National Technology & Engineering Solutions of Sandia, LLC, a wholly owned subsidiary of Honeywell International Inc., for the U.S. Department of Energy's National Nuclear Security Administration under contract DE-NA0003525.

dependence in a failure model that they then applied to oxygen-free high thermal conductivity (OFHC) copper, Armco iron, and 4340 steel [2]. Their model defines the fracture strain ($\bar{\varepsilon}_f$), for a material at a given temperature and loaded at a constant strain rate, as a monotonic function of the stress triaxiality, $\bar{\varepsilon}_f = C_1 + C_2 \exp(C_3 \eta)$. The stress triaxiality is defines as equal to $\sigma_m / \bar{\sigma}$, where the von Mises equivalent stress $\bar{\sigma}$ is equal to $\sqrt{3J_2}$ with J_2 being the second invariant of the deviatoric stress tensor. The remaining three parameters C_1, C_2, and C_3 are constants derived from fitting of the fracture strain function to data derived from torsion and uniaxial tension tests performed at various stress triaxialities. While the Johnson-Cook model is widely used and can successfully describe the response of various materials over a range of conditions, it does have limitations. Johnson and Cook observed that their model significantly overpredicted the fracture strain in torsion for the 4340 steel they investigated.

More recently, Xue and Wierzbicki have developed a ductile fracture failure model, referred to as the Xue-Wierzbicki or X-W model, that incorporates dependence of the fracture strain on the third invariant of the deviatoric stress tensor (J_3) through a variable they call the deviatoric state parameter ξ [3, 4]. Inclusion of dependence on J_3 enables the model to represent the behavior observed by Johnson and Cook for 4340 steel. The deviatoric state parameter ξ is related to J_3 and the Lode angle (θ) as follows.

$$\xi = \cos(3\theta) = \frac{27}{2} \frac{J_3}{\bar{\sigma}^3} \tag{1}$$

The X-W model postulates that fracture will occur when the accumulated plastic strain $\bar{\varepsilon}$, modified by a function $F(\eta,\xi)$, reaches a limiting value of one, as follow.

$$\int_0^{\bar{\varepsilon}_f} \frac{\mathrm{d}\bar{\varepsilon}}{F(\eta,\xi)} = 1 \tag{2}$$

Because the stress triaxiality and deviatoric state parameter vary during loading, average values of the parameters, defined below, are required to define a failure surface.

$$\eta_{av} = \frac{1}{\bar{\varepsilon}_f} \int_0^{\bar{\varepsilon}_f} \eta(\bar{\varepsilon}) \mathrm{d}\bar{\varepsilon}, \ \xi_{av} = \frac{1}{\bar{\varepsilon}_f} \int_0^{\bar{\varepsilon}_f} \xi(\bar{\varepsilon}) \mathrm{d}\bar{\varepsilon} \tag{3}$$

Evaluation of the failure integral (Eq. 2), using the average stress triaxiality and deviatoric parameter, yields $\bar{\varepsilon}_f = F(\eta_{av},\xi_{av})$. The X-W model assumes, based on experimental observations, that the fracture strain is bounded above by an axisymmetric stress state ($\xi_{av} = 1$) curve and below by a plane strain ($\xi_{av} = 0$) curve. These curves are represented in the model by the following assumed exponential functions.

$$\bar{\varepsilon}_f^{ax} = C_1 \mathrm{e}^{-C_2 \eta_{av}}, \qquad \xi_{av} = 1 \tag{4}$$

$$\bar{\varepsilon}_f^{ps} = C_3 \mathrm{e}^{-C_4 \eta_{av}}, \qquad \xi_{av} = 0 \tag{5}$$

The X-W model assumes the dependence of the fracture strain on the deviatoric state parameter ξ can be described by the following elliptic function

$$\left(\frac{\bar{\varepsilon}_f^{ax} - \bar{\varepsilon}_f}{\bar{\varepsilon}_f^{ax} - \bar{\varepsilon}_f^{ps}} \right)^{1/m} + \xi^{1/m} = 1 \tag{6}$$

where m is the closest even integer to $1/n$ where n is the power law hardening exponent for the material. Taken together, the fracture strain as a function of η_{av}, ξ_{av}, and n may be defined as follows.

$$\bar{\varepsilon}_f = F(\eta_{av},\xi_{av}) = C_1 \mathrm{e}^{-C_2\eta_{av}} - \left(C_1 \mathrm{e}^{-C_2\eta_{av}} - C_3 \mathrm{e}^{-C_4\eta_{av}}\right)\left(1 - \xi^{1/n}\right)^n \quad (7)$$

The four free parameters C_1, C_2, C_3, and C_4 are derived from coupon level material tests performed at differing stress triaxialities and deviatoric state parameter values.

MATERIAL TESTING

Mechanical tests were conducted [5, 6] to collect the data needed to build a X-W fracture model for PH13-8Mo H950. Tests were conducted at both 20 °C and -40 °C. Five test specimens of differing geometry (Figure 1) were used in the test campaign. The geometries of these specimens are identical to those described in reference [3]. These test specimens vary in both stress triaxiality and deviatoric state parameter as indicated in Table 2. Three of the specimen geometries (R5, 9 mm Notch, and 3 mm Notch) generate stresses with a deviatoric state parameter of approximately 1.0, while the remaining two specimens (Flat-Groove and Shear) generate stresses with a deviatoric state parameter of approximately 0.0. All test specimens were extracted from a cylindrical ring of material with their primary tensile axis oriented parallel to the axis of the cylinder. A duplicate set of R5 specimens were created from the same ring of material with their primary tensile axis oriented radially. This duplicate set of R5 specimens was used to characterize any anisotropy in the material response.

Figure 1. Test Specimen Geometries (Left to Right: R5, Flat-Groove, 9 mm Notch, 3 mm Notch, and Shear).

All specimens were tested in uniaxial tension using a servo hydraulic load frame. Applied load was measured using a 260 MN load cell, sub-ranged for specific tests to give more force precision. An environmental chamber attached to the load frame was used to perform testing at -40 °C. Strain was measured during testing using digital image correlation (DIC). Samples were loaded at rates between 0.008 mm/sec and 0.012 mm/sec depending on specimen type. For cold temperature tests, samples were first preloaded to a small amount of force and left to cool for approximately 30 minutes. During the cool down, actuator displacement was monitored until the displacement stabilized to assure that the load train had equilibrated to the oven temperature.

A summary of the mechanical properties derived from the testing is provided in Table 1. Figure 2 through Figure 6 illustrate the test setup and typical results obtained from the tests. Results from the R5 specimen testing showed minor differences in mechanical properties between the radial and axial directions, with the modulus of elasticity (E), ultimate tensile strength (UTS), and yield strength (YS) of the radial samples being 2% to 3% larger than for the axial samples. YS and UTS of both radial and axial samples increased with decreasing test temperature, ductility did not change significantly, and reduction in area decreased. Optical and scanning electron microscope (SEM) imaging of the fracture surfaces showed typical cup and cone fracture in all specimens, including those tested at -40 °C (Figure 2d and e). Cross-sections taken of the fracture surface show the presence of voids up to 500 μm below the fracture surfaces, indicating failure by void nucleation, growth, and coalescence.

Table 1. Summary of PH13-Mo H950 Mechanical Properties Derived From Testing.

Specimen Type	Temp.	Modulus of Elasticity (E)	Yield Stress (YS)	Ultimate Tensile Strength (UTS)	Ductility	Average Reduction in Area (RA)
	°C	GPa	MPa	MPa	%	%
R5 Axial	22	181 ± 1	1430 ± 22.7	1570 ± 16.0	12.8 ± 0.9	57.4
	-40	182 ± 4	1490 ± 7.9	1640 ± 3.7	12.0 ± 0.4	55.0
R5 Radial	22	185 ± 1	1470 ± 13.0	1600 ± 6.4	12.1 ± 0.3	55.7
	-40	186 ± 5	1530 ± 31.8	1660 ± 7.8	11.9 ± 0.7	48.6
9 mm Notch	22	-	1760 ± 1.4	1810 ± 1.8	5.6 ± 0.5	42.8
	-40	-	1820 ± 4.7	1900 ± 8.5	4.9 ± 0.8	31.6
3 mm Notch	22	-	1850 ± 37.1	2070 ± 6.9	7.6 ± 0.8	23.5
	-40	-	1930 ± 30.9	2170 ± 15.4	2.6 ± 0.3	5.8
Flat-Groove	22	-	1500 ± 63.9	1740 ± 14.8	7.3 ± 0.1	-
	-40	-	1410 ± 52.9	1840 ± 6.8	7.7 ± 0.5	-

The 9 mm notch test specimens exhibited modestly different mechanical behaviors at the two tested temperatures. The UTS and YS of specimens tested at -40 °C was 3% to 5% greater than those tested at 22 °C, whereas the ductility and RA were slightly lower. The fracture surfaces of the 9 mm notch specimens tested at both temperatures are characteristic of ductile, cup and cone fracture, with no significant differences observed between the fracture surfaces of specimens tested at 22 °C and -40 °C (Figure 3d and e).

The 3 mm notch test specimens exhibited significantly different mechanical behaviors at the two tested temperatures. While the UTS and YS at -40 °C was 4% to 5% greater than at 22 °C, the ductility was 66% lower and RA was 75% lower. Fracture surfaces of samples tested at 22 °C suggest ductile fracture, exhibiting cup and cone type failure (Figure 4d) like those observed in the R5 samples. Samples tested at -40 °C suggest ductile fracture, but also exhibit features reminiscent of brittle failure including indications of trans-granular fracture and significantly smaller shear lips (Figure 4e).

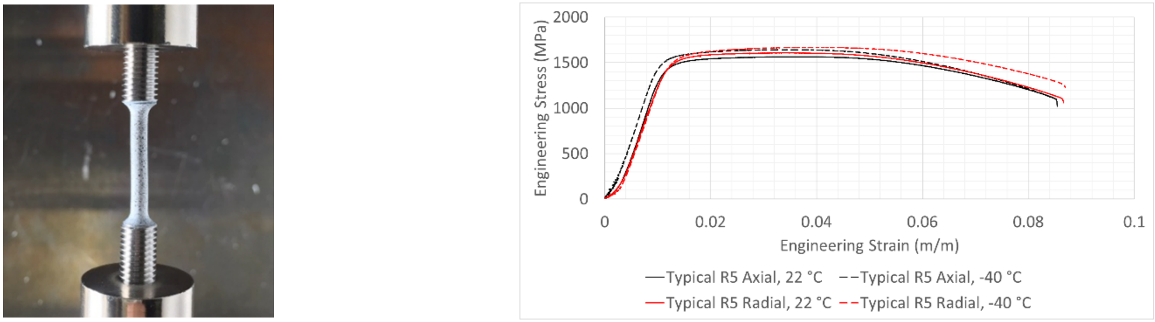

a) Test Setup

b) Stress-Strain Curves

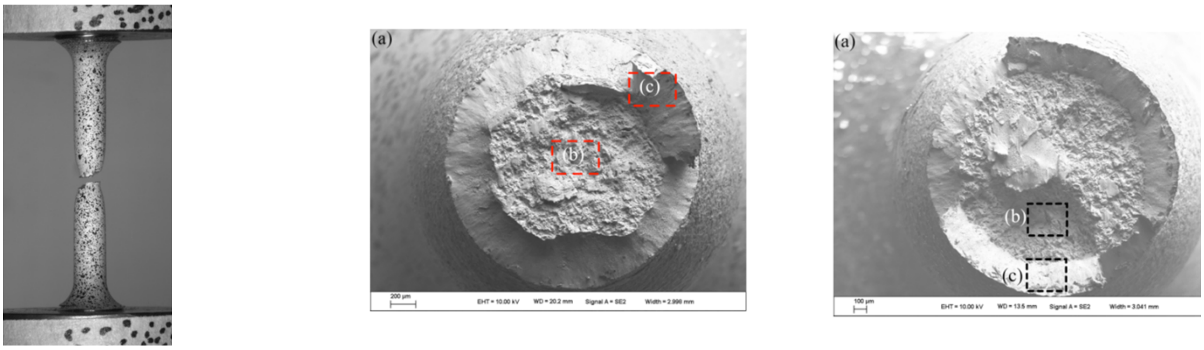

c) Fracture Location

d) Failure Surface of an R5 Specimen Tested at 22 °C

e) Failure Surface of an R5 Specimen Tested at -40 °C

Figure 2. R5 Specimen Test Setup and Typical Test Results.

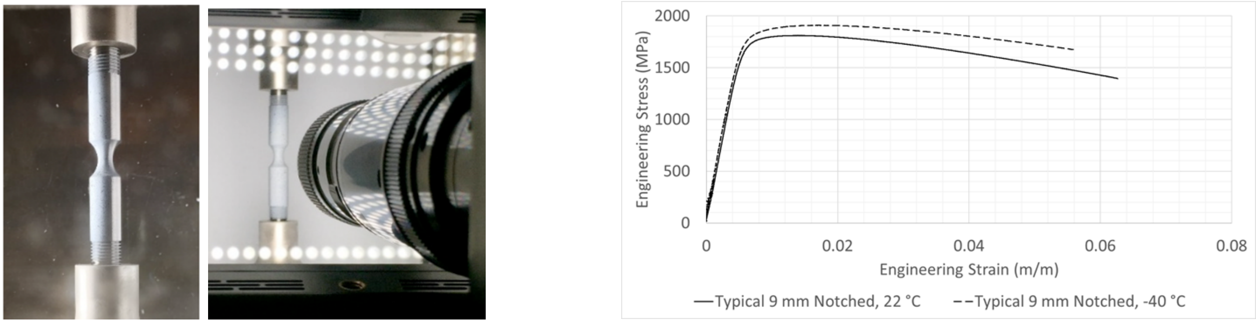

a) Test Setup

b) Stress-Strain Curves

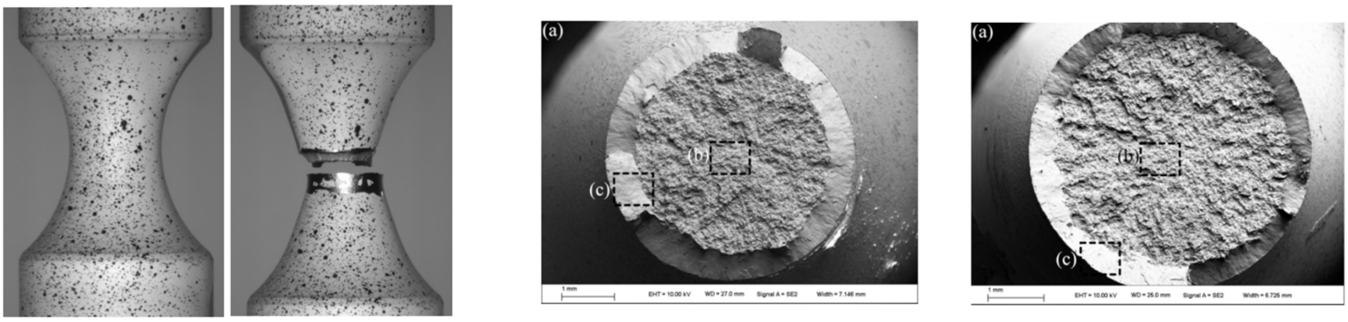

c) Fracture Location (22 °C)

d) Failure Surface of a 3 mm Notch Specimen Tested at 22 °C

e) Failure Surface of a 3 mm Notch Specimen Tested at -40 °C

Figure 3. 9 mm Notch Specimen Test Setup and Typical Test Results.

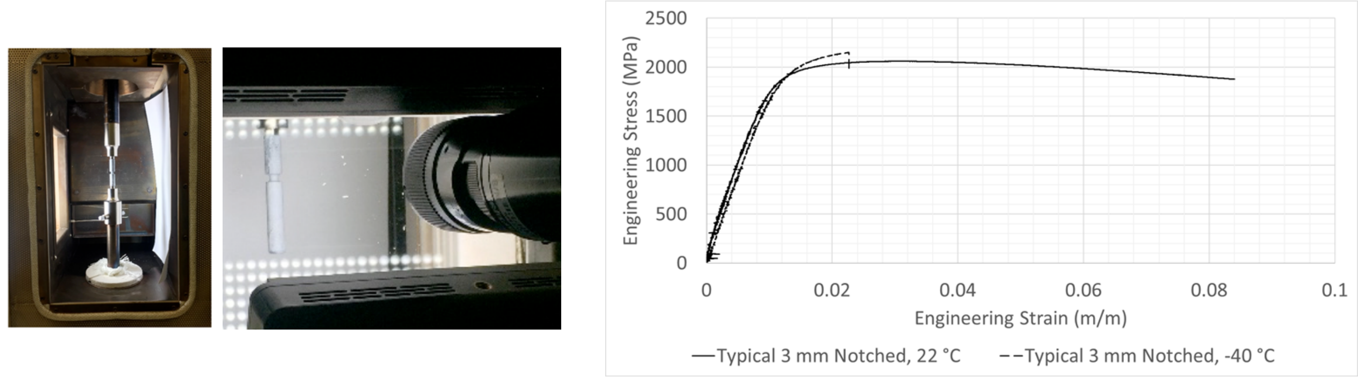

a) Test Setup

b) Stress-Strain Curves

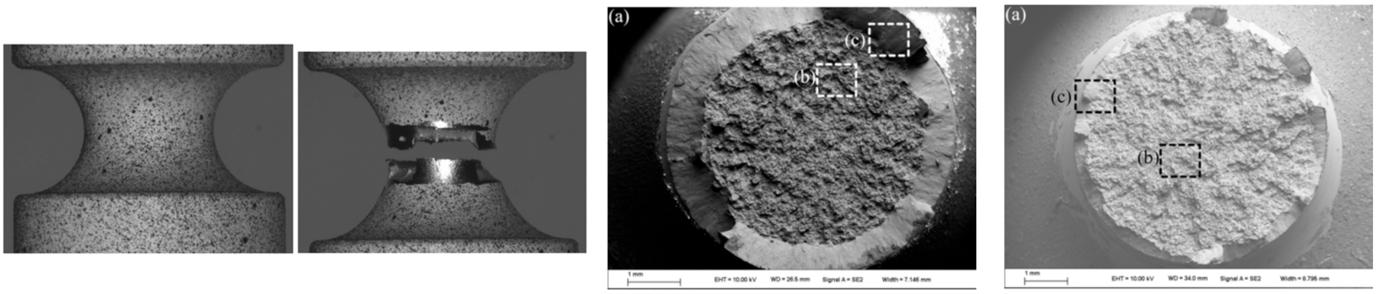

c) Fracture Location (22 °C)

d) Failure Surface of a 3 mm Notch Specimen Tested at 22 °C

e) Failure Surface of a 3 mm Notch Specimen Tested at -40 °C

Figure 4. 3 mm Notch Specimen Test Setup and Typical Test Results.

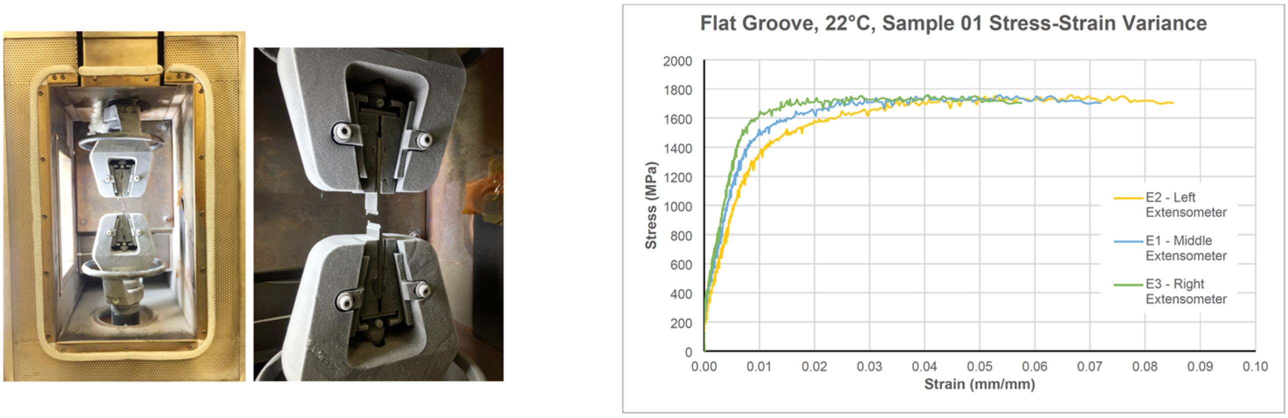

a) Test Setup

b) Stress-Strain Curves

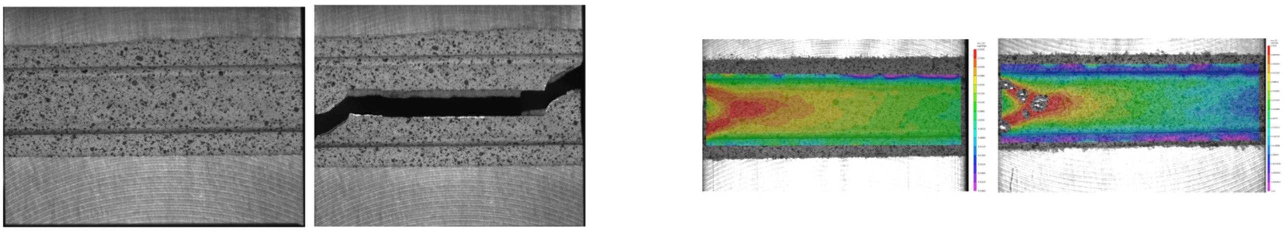

c) Fracture Location (22 °C)

d) Full Field Axial Strain Distribution (22 °C Left, -40 °C Right)

Figure 5. Flat-Grooved Specimen Test Setup and Typical Test Results.

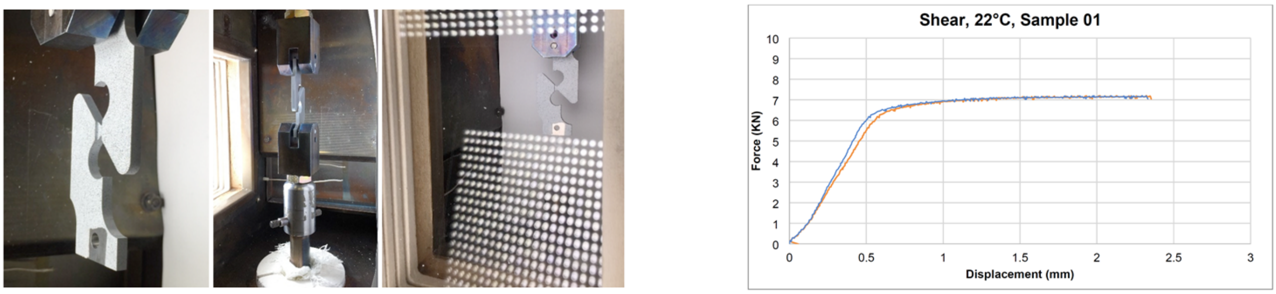

a) Test Setup

b) Force Displacement Curves

c) Fracture Location (22 °C)

d) Full Field Shear Strain Distribution (22 °C Left, -40 °C Right)

Figure 6. Shear Specimen Test Setup and Typical Test Results.

The flat-grooved specimens, like the other specimens tested, had an UTS at -40 °C approximately 4% greater than at 22 °C. The YS varied significantly (±4%) specimen-to-specimen so it is not possible to conclude if YS varied with temperature. Strain across the width of the specimen varied significantly (Figure 5d), with the strains differing across the width by 3% to 4%. Full-field strain data indicate strain localization would occur on one side of the sample before fracture (Figure 5d). Little difference was observed in the fracture surfaces of samples tested at 22 °C and -40 °C.

For the shear specimens, the ultimate tensile and yield forces increased with decreasing test temperature, with no measurable decrease in ductility. Shear dimples were observed across the fracture surfaces of specimens tested at both temperatures.

In general, fracture surfaces of all samples exhibited ductile failure features, including those from the 3 mm notch samples, although the 3 mm notch samples tested at -40 °C also included features typical of brittle cleavage, suggesting a combination of failure mechanisms. Images of the fracture surfaces of the 3 mm notch specimens indicate a transition in fracture mechanism from one dominated by void nucleation, growth, and coalescence at room temperature to a mix of brittle cleavage and void nucleation, growth, and coalescence at -40 °C. This suggest that the ductile-to-brittle transition temperature for PH13-8Mo H950 is near -40 °C.

FINITE ELEMENT ANALYSES

Finite element analyses were completed to extract the necessary information from the material test data to develop a X-W failure surface at room temperature and -40 °C. This consisted of a three-step process at each temperature. First hardening curves were developed by matching the response of a finite element model (FEM) with data from the R5 specimen tests. Second, using the hardening curves developed in the first step, FEM simulations of the remaining four specimen tests were completed and the relevant failure parameters extracted. Third, using the failure quantities derived in the second step, the four free parameters in Eq. 7 were determined for each temperature.

To develop the material hardening curves from the R5 specimen data, an automated fitting process was employed. FEM simulations were completed using the non-linear, implicit, transient-dynamics module within Sandia National Laboratories' Sierra Solid Mechanics (SIERRA/SM) finite element code [7]. Figure 7 shows the room temperature true-stress vs. true-strain hardening curve developed from the R5 specimen test data, and a comparison of the resulting force vs. displacement response of the FEM with the test data.

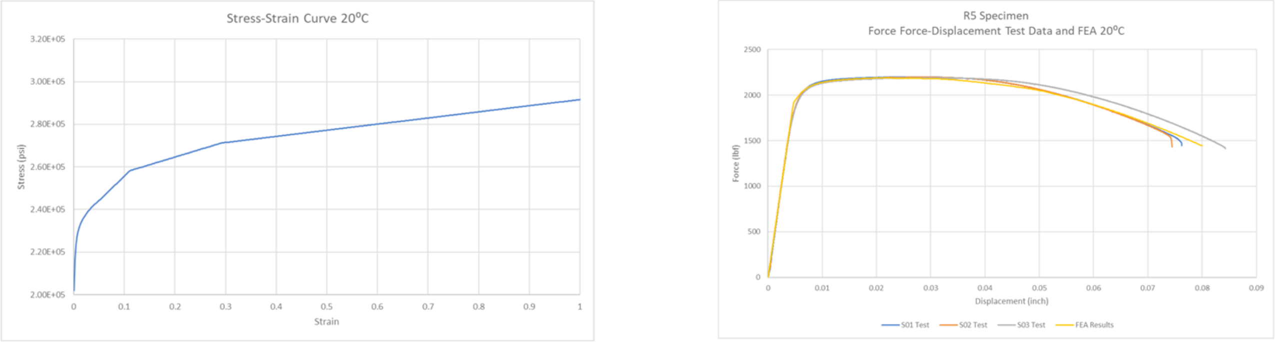

a) Hardening Curve.

b) Comparison of FEM and Test Data.

Figure 7. Room Temperature Hardening Curve Developed from R5 Tensile Test Data and Comparison of the Resulting FEM Response with the Test Data.

The derived hardening curves were incorporated into models for each of the remaining test specimens and peak equivalent plastic strain, average stress triaxiality, and average deviatoric parameter at failure determined. Table 2 summarizes these parameters. Using the values, coefficients for the X-W failure function (Eq. 7) were determined (listed in Table 3). Figure 8 shows a plot of the failure surfaces in η- ξ space. Because three tests with a ξ=1 were performed, and only two are required, there are at least three possible sets of $C1$ and $C2$ parameters that can be derived. At 20 °C, the exponential fit of Eq. 4 to all three data points is good, so the differences in $C1$ and $C2$ coefficients are minimal, regardless of which two data points are used to determine the coefficients. At -40 °C, this is not the case, with the $C1$ and $C2$ coefficients varying significantly based on which two sets of data are used. This indicates that the assumed exponential relationship inherent in Eq. 4, may not be valid for this material at -40 °C, particularly for the high stress triaxiality ($\xi > 0.8$) applicable to the 3 mm notch specimens.

Table 2. Average Stress Triaxiality, Deviatoric State Parameter, and Failure Strain for Each Test Specimen Geometry at 20 °C and -40 °C as Determined from the FE Analyses.

Specimen Name	20 °C			-40 °C		
	Stress Triaxiality (η)	**Deviatoric State Parameter (ξ)**	**Equivalent Plastic Strain at Failure**	**Stress Triaxiality (η)**	**Deviatoric State Parameter (ξ)**	**Equivalent Plastic Strain at Failure**
R5	0.593	1.0	0.892	0.605	1.0	0.867
9 mm Notch	0.785	1.0	0.520	0.767	1.0	0.296
3 mm Notch	1.095	1.0	0.190	0.878	1.0	0.018
Flat-Groove	0.578	0.0	0.194	0.556	0.0	0.078
Shear	0.0031	0.0	0.475	0.0033	0.0	0.488

Table 3. Derived X-W Failure Function Parameters.

Temperature (°C)	n	m	C1 and C2 Parameter Source	C1	C2	C3	C4
20	0.3488	2	R5, 3 mm	5.550	3.084	0.477	1.552
			R5, 9 mm	4.716	2.809	0.477	1.552
			9 mm, 3 mm	6.687	3.254	0.477	1.552
-40	0.3607	2	R5, 3 mm	4495.440	14.148	0.493	3.309
			R5, 9 mm	62.463	7.074	0.493	3.309
			9 mm, 3 mm	1.093e+07	23.030	0.493	3.309

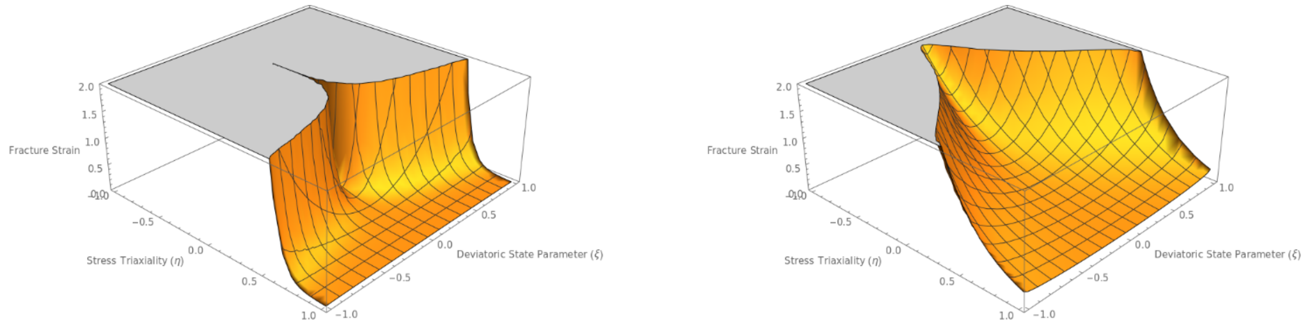

a) -40 °C (Based on R5, 3 mm Notch). b) Room Temperature (Based on R5, 3 mm Notch).

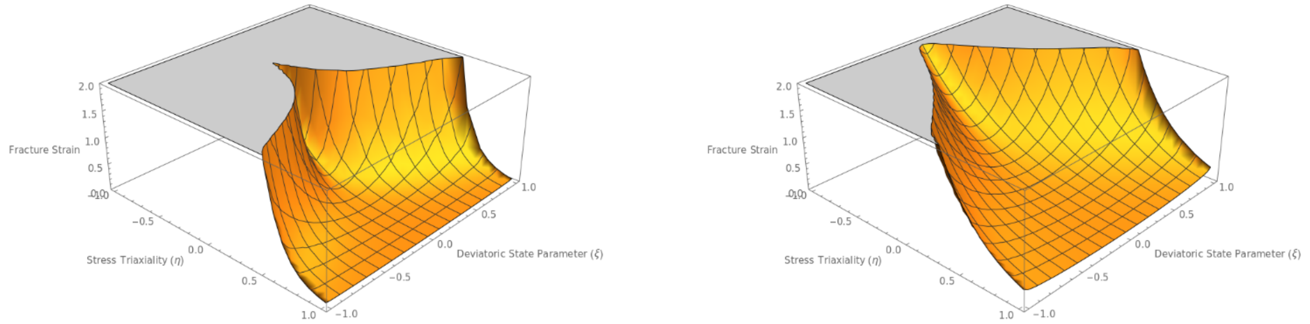

c) -40 °C (Based on R5, 9 mm Notch). d) Room Temperature (Based on R5, 9 mm Notch).

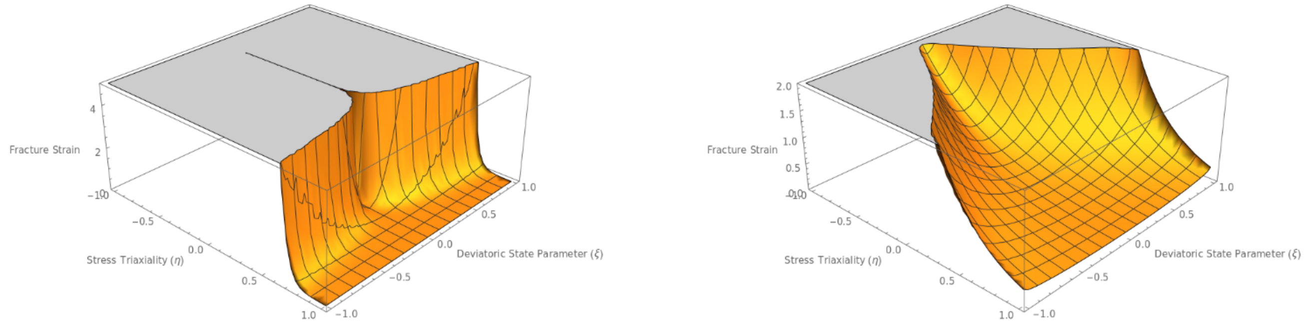

e) -40 °C (Based on 9 mm Notch, 3 mm Notch). b) Room Temperature (Based on 9 mm Notch, 3 mm Notch).

Figure 8. X-W Failure Surfaces.

SUMMARY AND CONCLUSIONS

Failure surfaces based on the X-W failure model have been developed for PH13-8Mo H950 steel at room temperature and -40 °C. Mechanical testing at those temperatures was conducted to collect the data needed to construct the failure surfaces, using five different test specimen geometries that vary in both stress triaxiality and deviatoric state parameter. Fracture surfaces on all specimens observed during testing exhibited features consistent with ductile failure mechanisms, with exception of the 3 mm notch samples tested at -40 °C which also demonstrated features of brittle cleavage, consistent with a combined ductile-brittle failure mechanism. This suggests that the ductile-to-brittle transition temperature for PH13-8Mo H950 steel is near -40 °C. Finite element modeling was employed to extract the necessary hardening behavior and failure parameters from the material test data. Using the FEM derived failure parameters, coefficients for X-W failure function were determined. It was observed that the assumed exponential relationship between stress triaxiality and fracture strain at deviatoric state parameter values of 1 provides a good fit to the test data at room temperature, but not at -40 °C, indicating that the assumption of an exponential relationship for this material at -40 °C may not be appropriate at high stress triaxiality (ξ>0.8), especially in light of the mixed ductile/brittle failure mechanism observed in the 3 mm notch specimen at -40 °C.

REFERENCES

1. Bridgman, Percy W. (1964). *Studies in Large Plastic Flow and Fracture, With Special Emphasis on the Effects of Hydrostatic Pressure*. Harvard University Press. https://doi.org/10.4159/harvard.9780674731349
2. Johnson, Gordon R., and Cook, William H. (1985). Fracture Characteristics of Three Metals Subjected to Various Strains, Strain Rate, Temperatures, and Pressures. *Engineering Fracture Mechanics*, 21(1), 31-48. https://doi.org/10.1016/0013-7944(85)90052-9
3. Wierzbicki, Tomasz, Bao, Yinbin, Lee, Young-Woong, and Bai, Yuanli (2005). Calibration and Evaluation of Seven Fracture Model. *International Journal of Mechanical Sciences*, 47(4-5), 719-743. https://doi.org/10.1016/j.ijmecsci.2005.03.003
4. Wierzbicki, T. and Xue, L. (2005). *On the Effect of the Third Invariant of the Stress Deviator on Ductile Fracture*. Report 136. Impact & Crash Worthiness Laboratory, MIT, Cambridge, Massachusetts, U.S.A.
5. Burgett, Chase R. (2018). *Material Testing of PH13-8Mo H950 Steel for Xue-Wierzbicki Fracture Criterion Determination*. SAND2018-10921. Sandia National Laboratories, Albuquerque, New Mexico, U.S.A.
6. Noel, Philip J., Pathare, Priya R., Casias, Zachary, Huber, Todd, Laing, John, and Carrol, Jay D. (2020). *Mechanical Testing of PH13-8Mo H950 Steel for Xue-Wierzbicki Fracture Criterion Determination at 20 °C and -40 °C*. SAND2020-5906. Sandia National Laboratories, Albuquerque, New Mexico, U.S.A.
7. Kalan, Robert J. (2021). *Development of a Ductile Rupture Failure Surface for PH13-8Mo H950 Steel Using the Xue-Wierzbicki Failure Model*. SAND2021-12191. Sandia National Laboratories, Albuquerque, New Mexico, U.S.A.
8. SIERRA Solid Mechanics Team (2021). *Sierra/SolidMechanics 5.0 User's Guide*. SAND2021-2961. Sandia National Laboratories, Albuquerque, New Mexico, U.S.A.